



Nickel-facilitated in-situ surface reconstruction on spinel Co_3O_4 for enhanced electrochemical nitrate reduction to ammonia

Lulu Qiao^a, Di Liu^a, Anquan Zhu^c, Jinxian Feng^a, Pengfei Zhou^a, Chunfa Liu^a, Kar Wei Ng^{a,*}, Hui Pan^{a,b,**}

^a Institute of Applied Physics and Materials Engineering, University of Macau, Macao SAR 999078, China

^b Department of Physics and Chemistry, Faculty of Science and Technology, University of Macau, Macao SAR 999078, China

^c Center of Super-Diamond and Advanced Films (COSDAF), Department of Materials Science and Engineering, City University of Hong Kong, Tat Chee Avenue, Kowloon, Hong Kong, China

ARTICLE INFO

Keywords:

Electrochemical nitrate reduction reaction (e-NO₃RR)
Spinel Co_3O_4
Ni-incorporation
Surface reconstruction

ABSTRACT

Transition metal oxides have shown efficient catalytic performance for electrochemical nitrate reduction reaction (e-NO₃RR). However, the surface evolution on catalyst remains elusive. Deciphering the dynamic evolution of electrocatalyst is pivotal for unveiling the catalytic origin and maximizing catalytic performance. Here, we report that incorporating nickel into Co_3O_4 can improve the electrocatalytic performance for e-NO₃RR to ammonia. Co_2NiO_4 shows excellent e-NO₃RR performance with a maximum Faraday efficiency of 94.9 % and NH_3 yield of $20 \text{ mg h}^{-1} \text{ cm}^{-2}$ at -1.0 V . Importantly, the reconstructed cobalt-nickel hydroxides ($\text{Co}_y\text{Ni}_{1-y}(\text{OH})_2$) on the surface of $\text{Co}_{3-x}\text{Ni}_x\text{O}_4$ is the active phase. DFT calculations confirm that $\text{Co}_y\text{Ni}_{1-y}(\text{OH})_2$ facilitates the formation of *NOH intermediate and suppresses HER. Our findings reveal that Ni-incorporation not only promotes the surface reconstruction, but also tunes the electronic structure of catalyst to improve the adsorption of intermediates and reduce the energy barrier. Our work may present a novel strategy to design electrocatalysts for e-NO₃RR.

1. Introduction

The production of ammonia (NH_3) by using renewable energy, referred as “green ammonia”, is considered as one of the promising routes for the international mission on carbon neutrality because the traditional way (Harsh-Barber method) consumes a lot of fossil fuels and releases a high amount of greenhouse gases [1–5]. At present, there have been several routes for producing “green ammonia”, such as photo/electrochemical reduction of nitrogen or nitrate to NH_3 [6–9]. Although green NH_3 can be produced via the electrocatalytic nitrogen reduction reaction (e-NRR) under ambient conditions, the yield and Faraday efficiency (FE) are very low due to its poor solubility and difficult activation [4–7,10]. Accordingly, e-NO₃RR has been considered as a promising way for the NH_3 production due to the lower dissociation energy of $\text{N}=\text{O}$ bonds and higher solubility of nitrate in aqueous solutions. Besides, nitrate widely exists in the wastewater from fertilizer, urban sewage, and industry emissions. The electrochemical conversion of nitrate into high-valued NH_3 therefore presents an alternative

approach for environmental remediation [11–13]. Hence, how to improve the efficiency for e-NO₃RR to be industrially applicable has attracted increasing attention, where the design of novel catalysts is the key.

To date, a variety of electrocatalysts, including carbon-based materials [12,14,15], alloys [16,17], metal oxides [2,18–25], and metal/polymer composites [1,26], have been developed for e-NO₃RR. In particular, spinel oxides have received intensive interest for e-NO₃RR due to their flexible ion arrangement, multivalent states, and high electrical conductivity [20,25,27–31]. Among those spinel oxides, Co_3O_4 is capable of selectively generating NH_3 through e-NO₃RR, but shows low NH_3 yield [29,32]. To improve the NH_3 yield of Co_3O_4 , many strategies have been applied, such as surface modulation [3,32,33], element incorporation [27,29,34], interface engineering [15,22,35]. The ion-replacement of Co at the tetrahedral or octahedral site in Co_3O_4 has been proved as one of the most effective approaches to regulate the local electronic structures and modulate the adsorption/desorption behaviors of intermediates for improved catalytic activity [25]. For

* Corresponding author.

** Corresponding author at: Institute of Applied Physics and Materials Engineering, University of Macau, Macao SAR 999078, China.

E-mail addresses: billyng@um.edu.mo (K.W. Ng), huipan@um.edu.mo (H. Pan).

example, Sun et al. reported that incorporation of Fe into Co_3O_4 boosted the adsorption of NO_3^- and inhibited the H_2 production, leading to higher NH_3 yield than pure Co_3O_4 [27]. They also reported that Ni-incorporated Co_3O_4 nanowires array (NiCo_2O_4) showed higher activity for e- NO_3RR than pure Co_3O_4 in alkaline solution because of the half-metallic property for the accelerated electron transfer and the switched rate determining step (RDS) with lower free energy [28]. Additionally, catalysts are subjected to surface reconstruction in most catalytic reactions [36–40]. For example, the surface of Co_3O_4 would convert to the CoOOH active phase through an electrochemical oxidation reaction with OH^- ions and water molecules in the oxygen evolution reaction (OER) [40]. Reconstruction has also been explored to develop highly active and stable electrocatalysts for e- NO_3RR [4,41,42]. For example, Wang et al. demonstrated that the active $\text{Cu}/\text{Cu}_2\text{O}$ phase converted from the CuO nanowire showed high NH_3 selectivity and FE because the electron transfer from Cu_2O to Cu at the interface could facilitate the formation of $^*\text{NOH}$ intermediate and suppress HER [41]. Similarly, $\text{Co}(\text{OH})_2$ was also reconstructed from CoP in e- NO_3RR [42]. However, there are few reports on the surface evolution and catalytic origin of Co_3O_4 -based catalysts in e- NO_3RR . Therefore, a thorough study on the roles of ion-incorporation and surface reconstruction is mandatory to understand the catalytic origin of Co_3O_4 for e- NO_3RR , which can

guide the design of the novel catalysts for enhanced catalytic performance.

Herein, $\text{Co}_{3-x}\text{Ni}_x\text{O}_4$ ($\text{Co}_{3-x}\text{Ni}_x\text{O}_4$, $x = 0, 0.5, 1, 1.5$) nanoarray on carbon cloth is presented as a highly efficient and robust electrocatalyst for e- NO_3RR with high selectivity and yield in neutral electrolyte. The as-obtained Co_2NiO_4 electrode achieves a maximum FE of 94.9 % with a NH_3 yield of $20 \text{ mg h}^{-1} \text{ cm}^{-2}$ at -1.0 V vs. RHE. Combining in-situ and ex-situ measurements, we demonstrate that the Ni-incorporation not only promotes the surface reconstruction of Co_3O_4 to $\text{Co}_y\text{Ni}_{1-y}(\text{OH})_2$, but also tunes its electronic structure. The DFT calculations show the Ni-incorporation can effectively optimize the adsorptions of intermediates on the reconstructed surface in e- NO_3RR , leading to high NH_3 yield and FE.

2. Experimental section

2.1. Synthesis of $\text{Co}_{3-x}\text{Ni}_x\text{O}_4$

The catalysts were prepared by a simple two-step method, that is, the hydroxide precursors with different Co/Ni molar ratios were prepared by a simple hydrothermal method, and then subsequently converted into $\text{Co}_{3-x}\text{Ni}_x\text{O}_4$ ($x = 0, 0.5, 1, 1.5$) and NiO through direct calcination in air

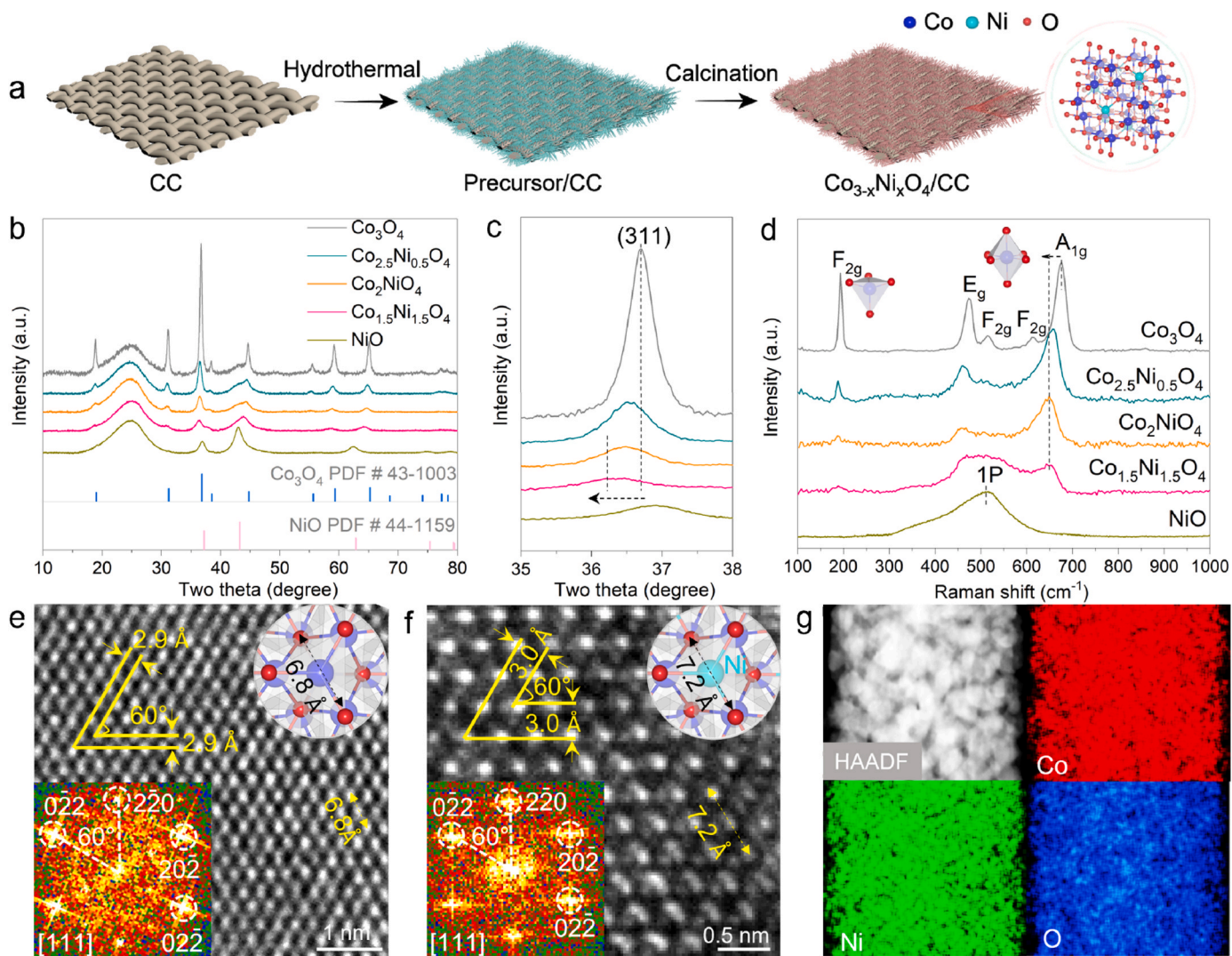


Fig. 1. Synthesis and Structural characterizations of $\text{Co}_{3-x}\text{Ni}_x\text{O}_4$. (a) Schematic illustration for the synthesis of $\text{Co}_{3-x}\text{Ni}_x\text{O}_4$. (b) XRD patterns and (c) the fine view of (311) peak for $\text{Co}_{3-x}\text{Ni}_x\text{O}_4$. (d) Raman spectra of $\text{Co}_{3-x}\text{Ni}_x\text{O}_4$. HRTEM images of pure Co_3O_4 (e) and Co_2NiO_4 (f), of which the insets are the corresponding FFT patterns and structural diagrams. (g) EDS elemental mappings of Co_2NiO_4 .

(Fig. 1a). In detail, carbon cloth (CC, 2.5 cm × 4 cm) as the substrate was successively immersed in piranha solution and deionized (DI) water for 15 min to remove the surface impurity. For a typical synthesis, 0.5 mmol nickel nitrate hexahydrate ($\text{Ni}(\text{NO}_3)_2 \cdot 6\text{H}_2\text{O}$) and 1 mmol cobalt nitrate hexahydrate ($\text{Co}(\text{NO}_3)_2 \cdot 6\text{H}_2\text{O}$) were firstly dissolved in 30 mL DI water. Then, 1 mmol ammonium fluoride (NH_4F) and 2 mmol urea ($\text{CH}_4\text{N}_2\text{O}$) were added to the above solution under magnetic stirring to obtain a homogeneous solution. After that, the mixture and treated CC were transferred into a 50 mL Teflon-lined autoclave, and kept at 120 °C for 12 h. The as-prepared cobalt nickel precursor ($\text{Co}_{3-x}\text{Ni}_x\text{-p}$) on CC was cut into 2.5 cm × 2 cm pieces and placed in a tube furnace. Then, the furnace was heated to 350 °C with a rate of 2 °C min⁻¹, and kept for 2 h in a N₂ atmosphere. The as-obtained sample was denoted as Co_2NiO_4 . $\text{Co}_{3-x}\text{Ni}_x\text{O}_4$ ($x = 0, 0.5, 1.5$) and NiO were also prepared by the same procedure (1.5 mmol $\text{Co}(\text{NO}_3)_2 \cdot 6\text{H}_2\text{O}$ for $x = 0$; 1.25 mmol $\text{Co}(\text{NO}_3)_2 \cdot 6\text{H}_2\text{O}$ and 0.25 mmol $\text{Ni}(\text{NO}_3)_2 \cdot 6\text{H}_2\text{O}$ for $x = 0.5$; 0.75 mmol $\text{Co}(\text{NO}_3)_2 \cdot 6\text{H}_2\text{O}$ and 0.75 mmol $\text{Ni}(\text{NO}_3)_2 \cdot 6\text{H}_2\text{O}$ for $x = 1.5$; 1.5 mmol $\text{Ni}(\text{NO}_3)_2 \cdot 6\text{H}_2\text{O}$ for NiO).

2.2. Materials characterization

Scanning electron microscopy (SEM) was performed using a Zeiss Sigma FESEM instrument. Transmission electron microscopy (TEM) was carried out on a Talos F200S equipment. The X-ray diffraction (XRD) was performed by the Rigaku SmartLab X-ray diffractometer equipped with the Cu K α radiation ($\lambda = 1.5418 \text{ \AA}$). The chemical composition and valence states were revealed by the X-ray photoelectron spectroscopy (XPS, Thermo Fisher Scientific, Al K α X-ray, $h\nu = 1486.7 \text{ eV}$, using C 1 s, 284.8 eV for calibration). The mass loadings of Co and Ni in $\text{Co}_{3-x}\text{Ni}_x\text{O}_4$ were measured by ICP-OES. The absorbance was recorded on the Shimadzu UV-2600 spectrophotometer (Tokyo, Japan). Raman spectroscopy was conducted by a Micro Raman System (Horiba LABHRV-UV) with the excitation source of 633 nm. For in-situ Raman measurement, a flow cell with three electrodes was used in conjunction with a Chenhua electrochemical workstation. While gradually changing the potential applied to the cell, the Raman spectra of the samples were obtained in turn.

2.3. Electrochemical measurements

All the electrochemical measurements were performed in a H-type cell with a typical three-electrode system linked with a ModuLab XM electrochemical workstation at room temperature, where self-supported catalyst (0.4 cm²), a Pt sheet and Ag/AgCl (saturated KCl) electrode were used as the working, counter, and reference electrodes, respectively. All the potentials in this work were converted to a reversible hydrogen electrode (RHE) by the formula of $E_{\text{RHE}} = E_{\text{Ag/AgCl}} + 0.197 \text{ V} + 0.059 \cdot \text{pH}$ [26].

The e-NO₃RR performance was carried out in an Ar-saturated neutral electrolyte ($\text{K}_2\text{SO}_4 + \text{KNO}_3$). To assess the influence of NO₃ concentration on the e-NO₃RR activity, 0.5 M K_2SO_4 was mixed with KNO_3 with concentration varying from 0.01 to 0.1 M. The linear sweep voltammetric (LSV) curves were measured with a scan rate of 5 mV s⁻¹ between 0.1 and -1.4 V vs. RHE. Polarization curves were obtained without iR-correction. The electrochemical impedance spectroscopy (EIS) and Bode plots were recorded at a frequency between 0.01 Hz and 100 KHz with an amplitude of 10 mV under different potentials. For investigating the FE and yield of NH₃, the chronoamperometry measurement (i-t curve) was applied at different potentials for 1 h. The durability of Co_2NiO_4 was performed at -1.0 V for 10 cycles. The HER performance was measured by LSV with a scan rate of 5 mV s⁻¹ in Ar-saturated 0.5 M K_2SO_4 solution. The double layer capacity (C_{dl} , mF cm⁻²) was calculated by a cyclic voltammetry (CV) method, where the CV scans were conducted at a potential range from 0.2 to 0.29 V with the increasing scan rates of 20, 40, 60, 80 and 100 mV s⁻¹. The capacitance current densities at 0.25 V were plotted against scan rates, and C_{dl} was

derived from the slope.

3. Results and discussion

3.1. Structural and composition characterization

The SEM images show that both the $\text{Co}_{3-x}\text{Ni}_x$ -hydroxide precursors and $\text{Co}_{3-x}\text{Ni}_x\text{O}_4$ are nanowires dominantly, and NiO is in the form of nanosheets (Figs. S1 & S2, Supporting Information). As the concentration of Ni increases, more nanosheets appear in $\text{Co}_{3-x}\text{Ni}_x\text{O}_4$. The XRD pattern of pure Co_3O_4 is well matched with the standard card of cubic spinel Co_3O_4 (JCPDS no. 43-1003), where a broad peak at around 26° is from the CC substrate (Fig. 1b) [43,44]. All the related peaks of Co_3O_4 slightly shift to lower diffraction angles after the Ni-incorporation. Specifically, the (311) peak exhibits the most significant shift (Fig. 1c), indicating that the Ni-substitution of partial Co sites gives rise to the lattice expansion [45]. Additionally, the peak intensity is reduced and the peak width is broadened, indicating the reduced crystallinity. Nevertheless, all $\text{Co}_{3-x}\text{Ni}_x\text{O}_4$ ($x \leq 1.5$) keep the cubic structure. The ICP-OES analyses show that the molar ratios of Co/Ni are 4.47:1, 1.73:1, and 0.86:1 for $\text{Co}_{2.5}\text{Ni}_{0.5}\text{O}_4$, Co_2NiO_4 , and $\text{Co}_{1.5}\text{Ni}_{1.5}\text{O}_4$, respectively (Fig. S2f, Supporting Information). Considering the minor difference between the theoretical and experimental results, we believe that Ni is easy to be incorporated uniformly into the lattice of Co_3O_4 .

The Raman scattering of Co_3O_4 (Fig. 1d) shows the vibration peaks of the octahedral $[\text{CoO}_6]$ units at ~470 cm⁻¹, 510 cm⁻¹, 610 cm⁻¹, and 680 cm⁻¹, which are indexed to the E_g, 2 F_{2g} and A_{1g} modes, respectively, and the peak of the tetrahedral $[\text{CoO}_4]$ units at ~190 cm⁻¹, which corresponds to the F_{2g} vibration mode [25,46,47]. The Raman peaks for the octahedral $[\text{CoO}_6]$ units in $\text{Co}_{3-x}\text{Ni}_x\text{O}_4$ exhibit an obvious blue shift, indicating the tension in the Co_3O_4 lattice with the Ni-incorporation [46], consistent with the XRD results. The peak area ratios of $[\text{CoO}_6]$ A_{1g} to $[\text{CoO}_4]$ F_{2g} are used to assess the substitution sites. The calculated ratios for Co_3O_4 , $\text{Co}_{2.5}\text{Ni}_{0.5}\text{O}_4$, Co_2NiO_4 , and $\text{Co}_{1.5}\text{Ni}_{1.5}\text{O}_4$ are 3.38, 10.50, 14.76, and 13.53, respectively, indicating that Ni mainly replaces the Co ion in the $[\text{CoO}_4]$ unit (Fig. S3, Supporting Information). Generally, the Co ions at the octahedral $[\text{CoO}_6]$ and tetrahedral $[\text{CoO}_4]$ units of Co_3O_4 are at the trivalent and bivalent states, respectively [48]. The XPS results show that the relative atomic ratios of trivalent/bivalent cobalt for Co_3O_4 , $\text{Co}_{2.5}\text{Ni}_{0.5}\text{O}_4$, Co_2NiO_4 and $\text{Co}_{1.5}\text{Ni}_{1.5}\text{O}_4$ are 1.30, 1.41, 1.52, and 1.82, respectively, indicating that the trivalent Co species in $\text{Co}_{3-x}\text{Ni}_x\text{O}_4$ increase with the increasing Ni-incorporation and further confirming that Ni is mainly in the tetrahedral unit (Fig. S4, Supporting Information), which is also consistent with our theoretical results (Fig. S5, Supporting Information). Besides, the binding energy of lattice oxygen (O_L) in Co_2NiO_4 obviously is lower than that in Co_3O_4 by ~0.6 eV (Fig. S4b, Supporting Information), and the concentration of defective oxygen (O_v) also increases as the Ni-incorporation increases, indicating that the Ni-incorporation modulates the local electronic potentials around the Co and O sites [49,50].

The TEM images (Fig. 1e-f, S6 & S7, Supporting Information) show that both Co_3O_4 and Co_2NiO_4 are nanowires composed of nanodomains (Figs. S6a & S7a, Supporting information). There are abundant grain boundaries and defects observed in the lattice of Co_2NiO_4 , while not observable in pure Co_3O_4 , suggesting that the Ni-incorporation reduces the crystallinity, which may facilitate the surface reconstruction (Figs. S6b & S7b, Supporting Information). High resolution TEM images taken along the [111] zone axis show that the interplanar spacings of (220) and (022) planes increase from 2.9 Å in Co_3O_4 to 3.0 Å in Co_2NiO_4 . The atomic distance between two specific Co sites (7.2 Å) in Co_2NiO_4 (marked by black arrow) is larger than that in Co_3O_4 (6.8 Å) (Figs. 1e, 1f & S7c, Supporting Information). These TEM results confirm the Ni-incorporation-induced lattice expansion in Co_3O_4 , in line with the XRD results. The EDS mappings show that the incorporated Ni ions are uniformly distributed over the Co_3O_4 matrix (Fig. 1g).

3.2. e-NO₃RR performance

The e-NO₃RR activities of Co_{3-x}Ni_xO₄ electrodes were tested to examine our design. The method of achieving ammonia quantification is available in [Supporting Information \(1. Product Quantification, Fig. S8\)](#). Firstly, we see that the Co_{3-x}Ni_xO₄ samples are poorer in HER than Co₃O₄ in 0.5 M K₂SO₄ ([Fig. S9, Supporting Information](#)), indicating that the Ni-incorporation effectively inhibits the HER activity, which may contribute to high selectivity for the NH₃ production. The current density of Co_{3-x}Ni_xO₄ in 0.5 M K₂SO₄ with KNO₃ is much larger than that in 0.5 M K₂SO₄ only because of the current induced by the nitrate reduction [8]. In particular, Co₂NiO₄ achieves the highest current density, indicating the best activity for e-NO₃RR ([Fig. S9, Supporting Information](#)). It shows higher NH₃ yield ($Y_{\text{NH}_3} = 13.24 \text{ mg h}^{-1} \text{ cm}^{-2}$) and FE value ($\text{FE}_{\text{NH}_3} = 94.04 \%$) than all the counterparts (especially Co₃O₄: $Y_{\text{NH}_3} = 11.05 \text{ mg h}^{-1} \text{ cm}^{-2}$, $\text{FE}_{\text{NH}_3} = 88.63 \%$) at -0.8 V vs. RHE , where the host Co₃O₄ shows the best FE value for the NH₃ synthesis ([Fig. 2a](#)). The optimal e-NO₃RR performance than all counterparts catalysts over Co₂NiO₄ is also demonstrated at -1.0 V vs. RHE ([Fig. S10, Supporting Information](#)). Therefore, the following discussion is focused on the comparative study between Co₃O₄ and Co₂NiO₄ ([Fig. 2 b & 2 c](#)). The electrolytes composed of 0.5 M K₂SO₄ solution with 10–100 mM KNO₃ were used to investigate the effect of nitrate concentration on the e-NO₃RR performance [16]. Clearly, the NH₃ yield and FE of Co₃O₄ and Co₂NiO₄ increase as the concentration increases, and Co₂NiO₄ always has better e-NO₃RR performance than Co₃O₄, confirming that the Ni-incorporation promotes the nitrate reduction within a wide concentration range of NO₃⁻ ([Fig. S11, Supporting Information](#)). The potential also affects the products in e-NO₃RR. Potential-dependent activity shows that Co₂NiO₄ has higher NH₃ yield and larger FE value than pure Co₃O₄ in the measured potential range ([Figs. S12 & S13, Supporting Information](#)). Co₂NiO₄ has the highest FE value up to 94.9 % (-1.0 V vs. RHE) and NH₃ yield of $27 \text{ mg h}^{-1} \text{ cm}^{-2}$ (-1.2 V vs. RHE), while the largest FE value and highest NH₃ yield for pure Co₃O₄ is 88.7 % at

-0.8 V vs. RHE , and $21.9 \text{ mg h}^{-1} \text{ cm}^{-2}$ at -1.2 V vs. RHE , respectively. The catalytic performance of Co₂NiO₄ in e-NO₃RR is comparable to or even better than those of most reported catalysts ([Table S1, Supporting Information](#)). Therefore, we can conclude that the Ni-incorporation intrinsically boosts the NH₃-production of Co₃O₄ in e-NO₃RR.

Since the electroreduction of nitrate (NO₃⁻) to NH₃ is a complex process involving the transfer of eight electrons, the by-products, such as NO₂⁻ and N₂H₄, are also studied by spectroscopy analysis ([Fig. S14, Supporting Information](#)) [51]. We find that the FE values of NO₂⁻ and H₂ for Co₂NiO₄ are only 0.17 % and 1.9 % at -1.0 V vs. RHE , implying that Co₂NiO₄ has excellent selectivity for the NH₃ production ([Figs. S15a & S16, Supporting Information](#)). The UV-Vis absorption spectra of N₂H₄ under different potentials are almost identical to that measured in blank electrolyte, confirming that N₂H₄ is not generated in e-NO₃RR ([Fig. S15b, Supporting Information](#)). At the same time, the NO₃⁻ removal rate on Co₂NiO₄ is higher than that on pure Co₃O₄ under different potentials, further indicating the role of Ni for the improved e-NO₃RR activity of spinel Co₃O₄ ([Figs. S17 & S18, Supporting Information](#)). The concentrations of NO₃⁻, NO₂⁻ and NH₄⁺ in electrolyte vary negligibly with no bias applied - suggest that there is no contamination from the testing setup, electrolyte, and our catalyst ([Fig. S19, Supporting Information](#)) [3,28]. The e-NO₃RR durability of Co₂NiO₄ was probed via chronoamperometric measurement at the potential (-1.0 V vs. RHE) with the highest NH₃ selectivity, and the electrolyte was refreshed hourly in first 10 h, as well as the 20th, 29th, and 44th h ([Fig. 2d](#)). After cycling for 45 h at -1 V vs. RHE , the NH₃ yield and FE value of Co₂NiO₄ are calculated to be $22.6 \text{ mg h}^{-1} \text{ cm}^{-2}$ and 94.1 %, respectively, indicating the high stability. Therefore, the Co₂NiO₄ may be practically applicable because of its excellent stability in e-NO₃RR. In addition, ¹⁵N isotope labeling experiments were performed and ammonia was identified by ¹H nuclear magnetic resonance (NMR) spectroscopy ([Fig. S20, Supporting Information](#)). Typical double peaks (at $\delta = 6.89$ and 7.13 ppm) of ¹⁵NH₄⁺ different from ¹⁴NH₄⁺ (Triple peaks at $\delta = 6.84$, 7.01 and 7.18 ppm) appear in the ¹H NMR spectra, where the peaks detected

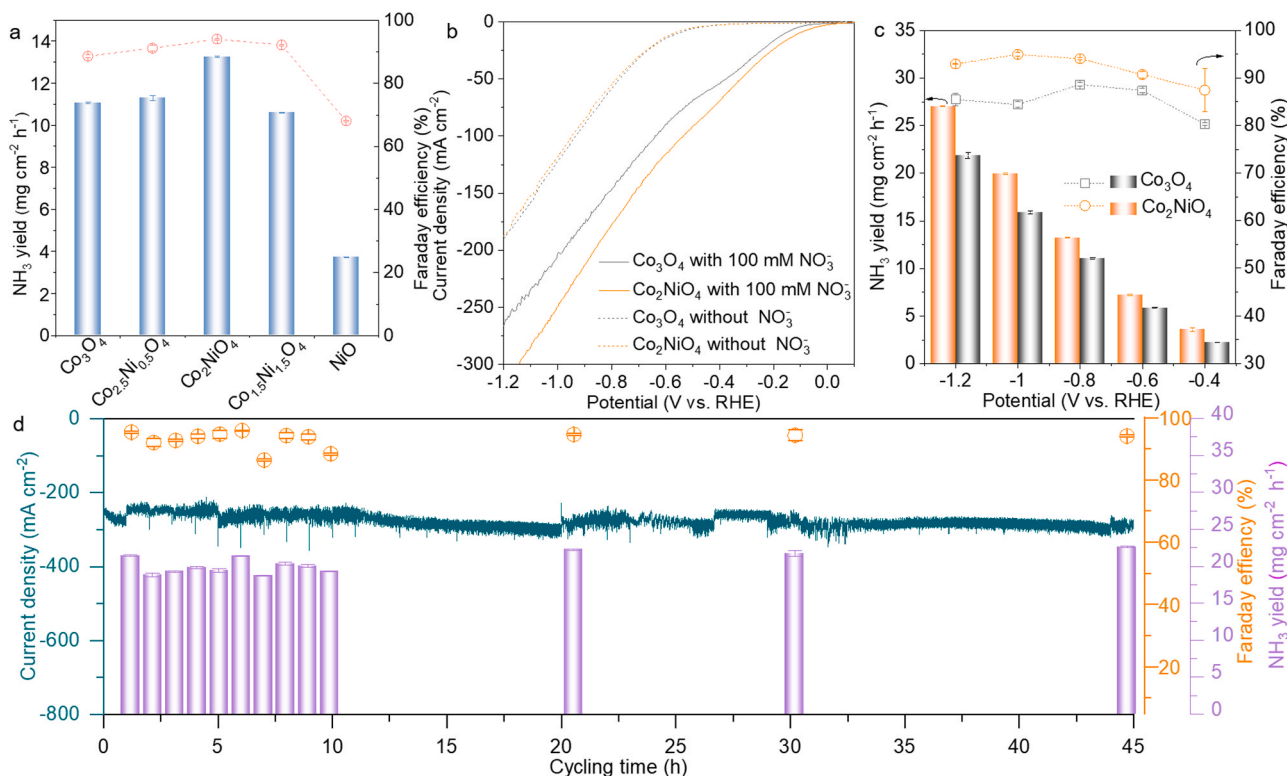


Fig. 2. e-NO₃RR performance. (a) NH₃ yields and FEs of different samples at -0.8 V vs. RHE . (b) LSV curves of Co₃O₄ and Co₂NiO₄ in 0.5 M K₂SO₄ with/without 0.1 M KNO₃. (c) NH₃ yields and FEs of Co₂NiO₄ and Co₃O₄ at different potentials. (d) The current densities, NH₃ yields and FEs at -1.0 V vs. RHE for 45 h.

from electrolytes using $^{14}\text{NO}_3^-$ and $^{15}\text{NO}_3^-$ reactants show the similar chemical shifts to the standard $^{14}\text{NH}_4\text{Cl}$ and $^{15}\text{NH}_4\text{Cl}$, respectively. Therefore, the detected NH_3 is originated from e- NO_3RR catalyzed by Co_2NiO_4 .

3.3. e- NO_3RR kinetics

The electrochemical impedance spectroscopy (EIS) is well-recognised as an effective tool to understand the catalytic kinetics [52–54]. In-situ Nyquist plots for both Co_3O_4 and Co_2NiO_4 were performed (Figs. S21 & S22, Supporting Information). The equivalent circuit model is demonstrated too, where R_s , R_{ct} and CPE are the solution resistance, charge transfer resistance, and constant phase element, respectively [55,56]. We see that the R_s value during e- NO_3RR decreases with increasing potential (Fig. 3a), because the e- NO_3RR process releases a lot of intermediate ions/groups into the electrolyte, e.g. NH_4^+ , NO_2^- , et al., which facilitate the charge transfer in the electrolyte. Differently, the R_s value during HER maintains the same (Fig. S21g, Supporting Information). Obviously, Co_2NiO_4 shows much lower R_{ct} value, higher response frequency, and lower angle of phase peak in Bode plots under the same potential than pure Co_3O_4 (Fig. 3b & 3c), indicating that the Ni-incorporation effectively accelerates the e- NO_3RR kinetics in neutral media [25]. The competition between e- NO_3RR and HER on the Co_2NiO_4 electrode was also investigated. In the electrolyte without (w/o) nitrate, the phase peaks at low-frequency region (10^{-2} – 10^0 Hz) attribute to the surface H^+ during HER, which starts at -0.4 V vs. RHE (Fig. 3d & S22, Supporting Information) [54], while the phase peaks shift to the medium-frequency region (10^0 – 10^2 Hz) during e- NO_3RR , involving the adsorption of complex reactant/intermediates [57]. The broad peak within 10^{-2} – 10^2 Hz at -0.1 V shows a relatively low potential to initiate the nitrate reduction [25]. The phase peaks in

the medium-frequency region (10^1 – 10^2 Hz) with low phase angle at -0.4 V and -0.7 V indicate the dominant and fast e- NO_3RR process on the Co_2NiO_4 electrode [52]. Both Co_3O_4 and Co_2NiO_4 have similar C_{dl} values, indicating that the Ni-incorporation improves the intrinsic activity towards e- NO_3RR rather than surface area (Fig. S23, Supporting Information). Therefore, we see that the Ni-incorporation can boost the e- NO_3RR kinetics of Co_3O_4 , which is conducive to high NH_3 yield and FE.

3.4. Active phase

To understand the enhanced e- NO_3RR activity over the Co_2NiO_4 electrode, comprehensive characterizations were performed and analyzed. After the chronoamperometry test, Co_3O_4 and Co_2NiO_4 basically remain as nanowire with rough surface, indicating a surface reconstruction during e- NO_3RR (Figs. S24 & S25, Supporting Information). The XRD patterns show that the diffraction peaks of Co_2NiO_4 are weaker after e- NO_3RR than those before the test, and a new and weak diffraction peak appears at $\sim 51^\circ$, corresponding to the (102) plane of $\text{Co}(\text{OH})_2$ (JCPDS 30-0443) (Fig. 4a & S25a, Supporting Information) [58]. TEM images reveal the loose surface of Co_2NiO_4 is composed of abundant wrinkles (Fig. 4b). The enlarged images (Region I and III) show that the reconstructed nanosheets have low crystallinity and rich defects, and the interplanar spacing of 2.4 \AA can be indexed to the (101) plane of $\text{Co}(\text{OH})_2$, consistent with the XRD results (Fig. 4c & 4e). The core of Co_2NiO_4 (Region II) keeps unchanged after e- NO_3RR (Fig. 4c & 4d), indicating that the reconstruction happens at the surface [59,60]. The reconstructed nanosheets are further confirmed to be nickel-cobalt hydroxide ($\text{Co}_y\text{Ni}_{1-y}(\text{OH})_2$) from the uniform distribution of Co, Ni, and O elements over the whole nanosheet (Fig. 4f). The high-resolution Co 2p and Ni 2p XPS spectra of Co_2NiO_4 after e- NO_3RR reveal that the

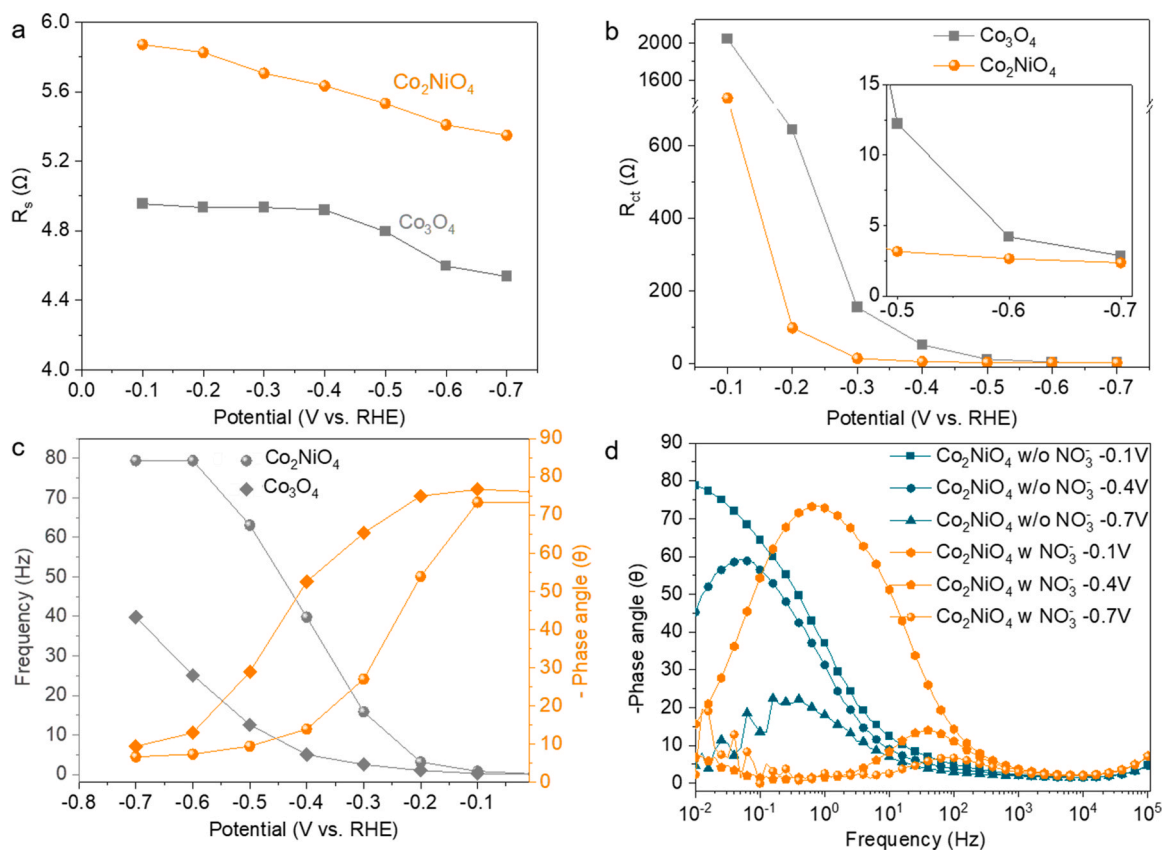


Fig. 3. Analysis of kinetics. (a) The fitted solution resistance (R_s) of electrolyte (0.5 M K_2SO_4 & 0.1 M KNO_3) and (b) charge transfer resistance (R_{ct}) for Co_2NiO_4 and Co_3O_4 at different potentials during e- NO_3RR . (c) Potentials dependent frequencies and phase angles for Co_2NiO_4 and Co_3O_4 . (d) Bode plots of Co_2NiO_4 at different potentials with/without KNO_3 .

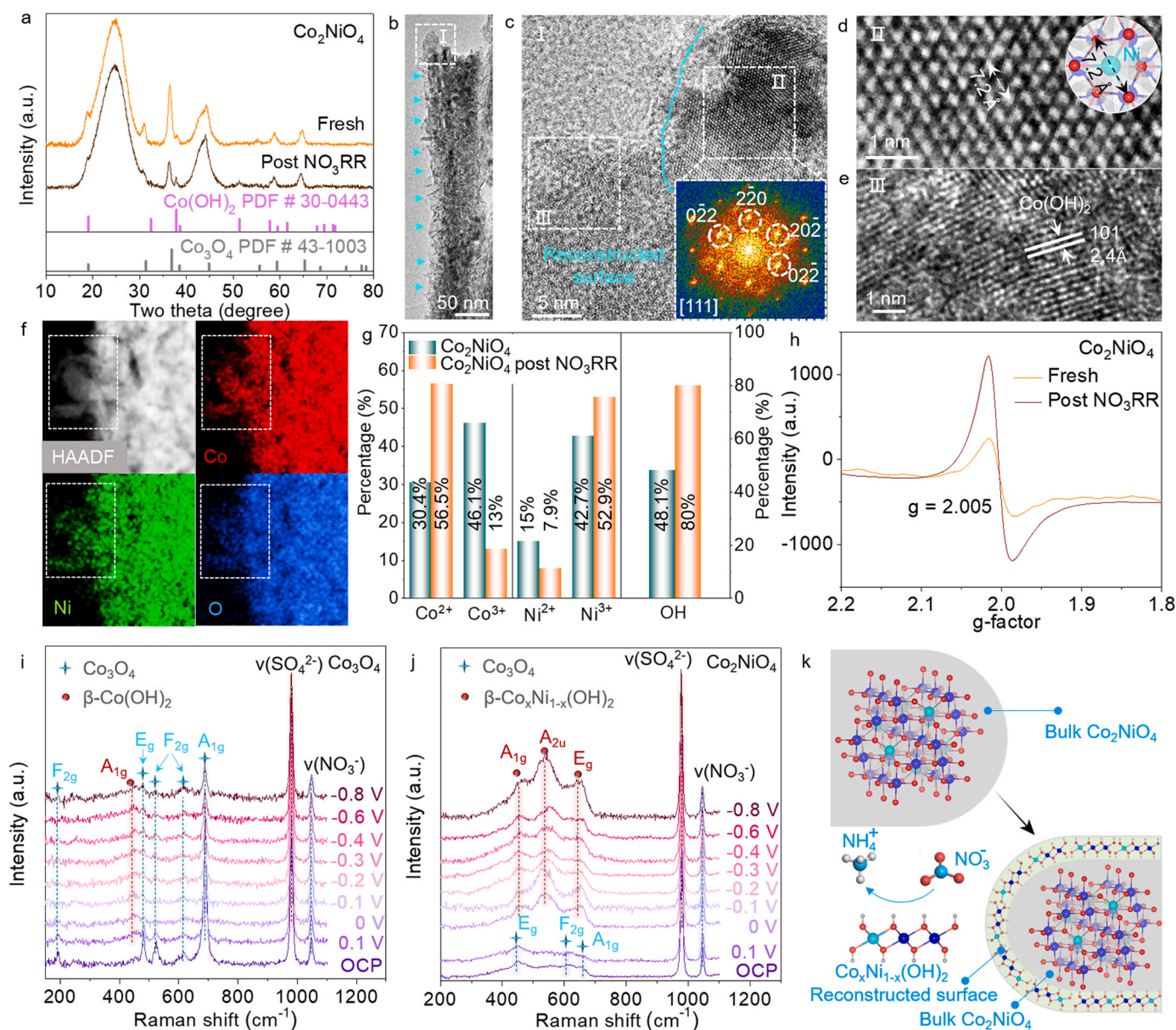


Fig. 4. Characterizations and illustration of surface reconstruction. (a) XRD patterns of Co_2NiO_4 before and after e- NO_3RR . (b) TEM and (c) HRTEM images at the specific area I in (b) (the inset is the corresponding FFT pattern of Region II), (d) and (e) HRTEM images at the specific areas II and III in (b), and (f) EDS elemental mappings of Co_2NiO_4 after e- NO_3RR . (g) The relative contents of different Ni and Co species from the Co $2p_{3/2}$ and Ni $2p_{3/2}$ XPS spectra for Co_2NiO_4 before and after e- NO_3RR . (h) EPR spectra of Co_2NiO_4 before and after e- NO_3RR . Potential-dependent in-situ Raman spectroscopy of (i) Co_3O_4 and (j) Co_2NiO_4 in 0.5 M K_2SO_4 with 0.1 M KNO_3 . (k) The schematic illustration for the surface reconstruction on the Co_2NiO_4 electrode during e- NO_3RR .

relative contents of Co^{2+} and Ni^{3+} increase, indicating valence changes induced by the surface reconstruction (Fig. 4g & S26, Supporting Information). The O 1s XPS spectrum shows that the content of -OH (O2) (80 %) in Co_2NiO_4 after e- NO_3RR is much higher than that in the fresh one (48.1 %), confirming the surface reconstruction from oxide to hydroxide. The intensity of EPR peak in Co_2NiO_4 after e- NO_3RR is higher than that of original electrode, indicating there are more unsaturated coordination bonds in the tested electrode, which may be more conducive to the catalytic reaction (Fig. 4h) [47].

In-situ Raman spectroscopy was employed to monitor the surface evolution during e- NO_3RR (Fig. 4i & 4j). The ex-situ Raman spectra show that both Co_3O_4 and Co_2NiO_4 have the characteristic peaks of F_{2g} , E_g and A_{1g} modes [61]. As the electrodes are immersed into K_2SO_4 electrolyte with KNO_3 (Open-circuit potential, OCP), the intensity and position of the above Raman peaks change obviously due to the difference between in situ and ex-situ Raman testing conditions (Figs. 1d, 4i &

4j). The intensities of peaks at 477 (E_g), 523 (F_{2g}), 620 (F_{2g}) and 687 cm^{-1} (A_{1g}) gradually decrease as the negative potential decreases (0.1 to -0.8 V vs. RHE) because of the gradual reconstruction of Co_3O_4 under a reduction process (Fig. 4i). Importantly, a new broad peak at around 450 cm^{-1} appears at -0.1 V, which is attributed to the characteristic peak A_{1g} mode of $\beta\text{-Co}(\text{OH})_2$. For the Co_2NiO_4 electrode, the Raman active modes related to the Co/Ni oxides disappear at 0 V. Meanwhile, three new and evident peaks with respective to the A_{1g} , A_{2u} and E_g modes of $\text{Co}_y\text{Ni}_{1-y}(\text{OH})_2$ are observed [62], indicating the Ni-incorporation facilitates the reconstruction from oxide to hydroxide (Fig. 4j). In addition, the A_{1g} peak at 687 cm^{-1} gradually shifts to 692 cm^{-1} with increasing potential, which is attributed to the adsorption of molecules or intermediates on the surface of catalyst [63]. These findings clearly demonstrate that the surface reconstruction from oxide to hydroxide ($\beta\text{-Co}(\text{OH})_2$ or $\text{Co}_y\text{Ni}_{1-y}(\text{OH})_2$) occurs during e- NO_3RR , and the reconstructed hydroxides are actually the active phases

(Fig. 4k).

3.5. Theoretical calculation

To disclose the e-NO₃RR reaction paths and reveal the mechanism on the Co₂NiO₄ electrode, we carried out theoretic calculations based on density-functional theory (DFT) (Fig. 5). Our systematical characterizations show that Co_{3-x}Ni_xO₄ actually acts as precatalyst, and undergoes surface reconstruction during e-NO₃RR to form hydroxides (Co(OH)₂ or Co_yNi_{1-y}(OH)₂), which are the active phase. Based on the HRTEM images (Fig. 4d), the (101) surfaces for both Co(OH)₂ and Ni-Co(OH)₂ were used as the model to investigate the catalytic performances of HER and e-NO₃RR. For HER, *H prefers to adsorb on O sites at the surfaces for both Co(OH)₂ and Ni-Co(OH)₂ (Fig. 5a). The Gibbs free energies for the adsorption of *H on Co(OH)₂ and Ni-Co(OH)₂ are -0.15 eV and -0.58 eV, respectively, indicating the surface sites on Ni-Co(OH)₂ are less active than those on Co(OH)₂ for HER (Fig. 5b). For e-NO₃RR, the adsorption of NO₃⁻ to generate reactive NO₃* species is the first step, followed by hydrodeoxygenation to generate NO₂*. Then, NO₂* is hydrodeoxygenated to NO* [16]. There are three e-NO₃RR pathways: NOH pathway from *NO to *NOH (*NOH → *N → *NH → *NH₂ → *NH₃) and two NHO pathways from *NO to *NHO (*NHO → *NHOH → *NH₂OH → *NH₂ → *+NH₃ and *NHO → *NH₂O → NH₃ + *O → *OH → *+H₂O) [42]. The Gibbs free energy from NO₃⁻ to NO₃* on Ni-Co(OH)₂ (-2.46 eV) is more negative than that on Co(OH)₂

(-2.27 eV), indicating stronger adsorption ability of Ni-Co(OH)₂ for NO₃⁻ reactant in e-NO₃RR. For Co(OH)₂, the rate-determining step (RDS) is *NO → *NHO with an uphill ΔG of 0.29 eV, and then NH₃ is produced by three hydrogenation processes (Fig. 5c, Gray lines). After incorporating Ni, the reaction path switches from *NO → *NHO to *NO → *NOH, and the most endothermic step is the step from *NO → *NOH, which has a much lower ΔG (-0.23 eV). Therefore, our DFT study reveals that the Ni-incorporation can inhibit the HER performance and improve the e-NO₃RR activity, in accordance with the experimental observations. (Fig. 5c, red lines).

Combining experimental and theoretical observations, we highlight: (1) the Ni-incorporation into Co₃O₄ can promote the surface reconstruction from Co_{3-x}Ni_xO₄ to hydroxides, and (2) the as-reconstructed Co_yNi_{1-y}(OH)₂ inhibits HER, and switches the e-NO₃RR paths from the uphill *NO → *NHO (RDS, ΔG: 0.29 eV) to the energetically favorable *NO → *NOH (ΔG: -0.23 eV). As a consequence, the Co₂NiO₄ catalyst with reconstructed Co_yNi_{1-y}(OH)₂ surface shows superior NH₃ yield and selectivity in e-NO₃RR.

4. Conclusion

In summary, Co_{3-x}Ni_xO₄ is demonstrated to be an effective precatalyst for selective NH₃-production in e-NO₃RR. The Co₂NiO₄ electrode exhibits the best e-NO₃RR performance with a maximum FE of 94.9 % and corresponding NH₃ yield of 20 mg h⁻¹ cm⁻² at -1.0 V vs.

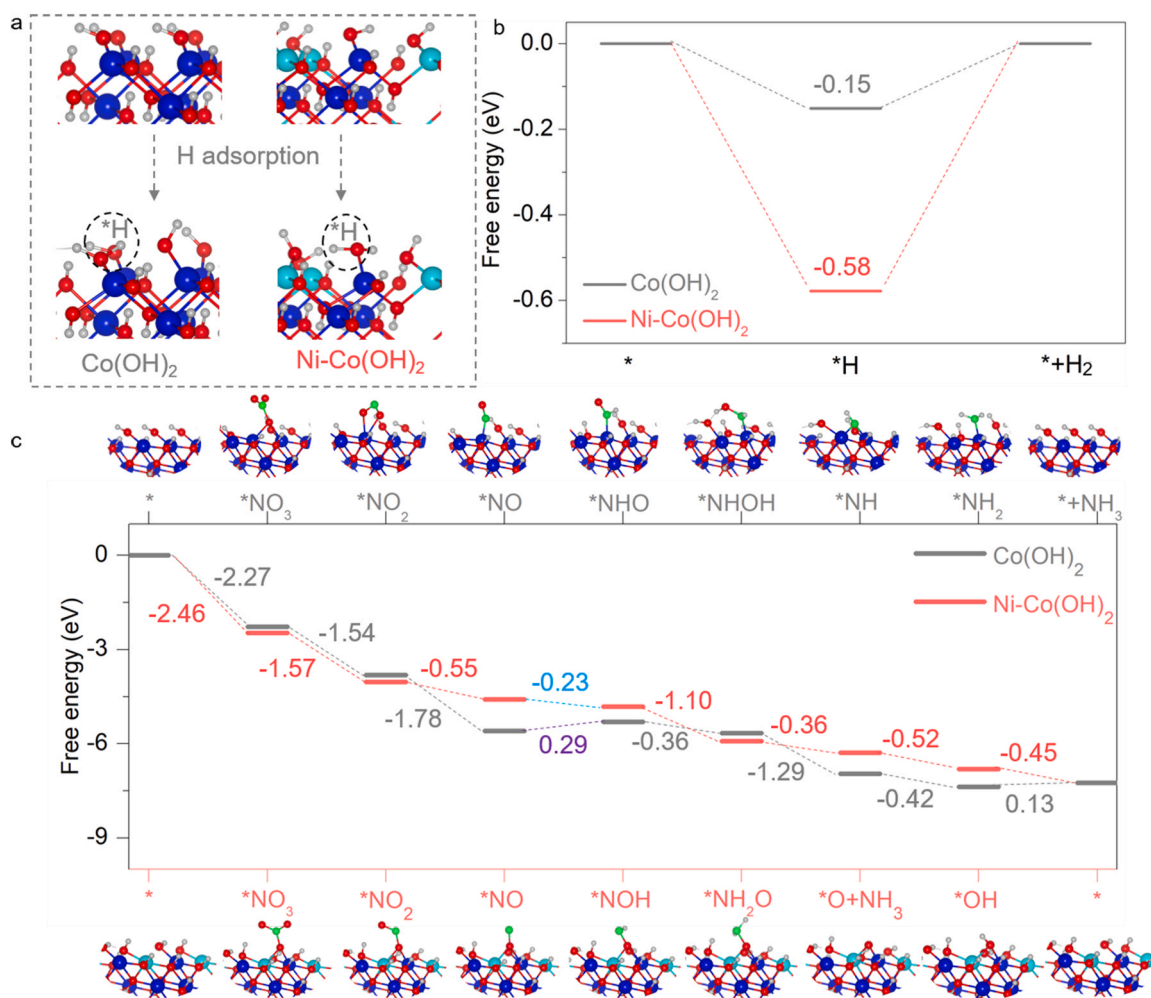


Fig. 5. DFT calculations. (a) The structure models of H adsorption on the O sites of Co(OH)₂ (101) and Ni-incorporated Co(OH)₂ (101) slabs (color notation: dark blue-Co, red-O, and cyan-blue-Ni). (b) The energy profiles for HER on pure and Ni-incorporated Co(OH)₂. (c) The energy profiles for e-NO₃RR on pure and Ni-incorporated Co(OH)₂.

RHE in neutral media. Importantly, we reveal that the surface of spinel $\text{Co}_{3-x}\text{Ni}_x\text{O}_4$ is easier to be reconstructed to $\text{Co}_y\text{Ni}_{1-y}(\text{OH})_2$ during $\text{e-NO}_3\text{RR}$, because the Ni-incorporation can modulate the electronic structure of Co_3O_4 . We find that the reconstructed surface serves as the active phase for the nitrate-to-ammonia conversion and $\text{Co}_y\text{Ni}_{1-y}(\text{OH})_2$ is more effective than $(\text{Co}(\text{OH})_2)$ because of the improved kinetics and selectivity. Our DFT calculations further certify that the Ni-incorporation in $\text{Co}(\text{OH})_2$ suppresses HER, and switches the reaction paths from uphill $^*\text{NO} \rightarrow ^*\text{NHO}$ (RDS, ΔG : 0.29 eV) to energetically favorable $^*\text{NO} \rightarrow ^*\text{NOH}$ (ΔG : -0.23 eV), leading to superior $\text{e-NO}_3\text{RR}$ performance. Our work demonstrates the dynamic reconstruction of spinel oxides to hydroxides as catalytically active phase during $\text{e-NO}_3\text{RR}$, providing insightful understanding for the design of electrocatalysts with high efficiency.

CRediT authorship contribution statement

Lulu Qiao: Conceptualization, Investigation, Writing – original draft; **Di Liu**: Investigation, Validation, Writing – review & editing; **Anquan Zhu**: Investigation, Writing – review & editing; **Jinxian Feng**: Validation, Visualization; **Pengfei Zhou**: Validation, Visualization; **Chunfa Liu**: Visualization; **Kar Wei Ng**: Funding acquisition, Writing – review & editing; **Hui Pan**: Conceptualization, Funding acquisition, Writing – review & editing.

Declaration of Competing Interest

The authors declare that they have no known competing financial interests or personal relationships that could have appeared to influence the work reported in this paper.

Data availability

Data will be made available on request.

Acknowledgements

This work was supported by the Science and Technology Development Fund (FDCT) from Macau SAR (0081/2019/AMJ, 0154/2019/A3, 0052/2021/AGJ, 006/2022/ALC, and 0111/2022/A2) Multi-Year Research Grants (MYRG2020-00026-FST and MYRG2022-00026-IAPME) from Research & Development Office at University of Macau, and Shenzhen-Hong Kong-Macao Science and Technology Research Programme (Type C) (SGDX20210823103803017) from Shenzhen. The DFT calculations were performed at the High Performance Computing Cluster (HPCC) of the Information and Communication Technology Office (ICTO) at the University of Macau.

Appendix A. Supporting information

Supplementary data associated with this article can be found in the online version at [doi:10.1016/j.apcatb.2023.123219](https://doi.org/10.1016/j.apcatb.2023.123219).

References

- [1] Y. Xu, Y. Wen, T. Ren, H. Yu, K. Deng, Z. Wang, X. Li, L. Wang, H. Wang, Engineering the surface chemical microenvironment over CuO nanowire arrays by polyaniline modification for efficient ammonia electrosynthesis from nitrate, *Appl. Catal. B: Environ.* 320 (2023), 121981, <https://doi.org/10.1016/j.apcatb.2022.121981>.
- [2] Z. Gong, W. Zhong, Z. He, C. Jia, D. Zhou, N. Zhang, X. Kang, Y. Chen, Improving electrochemical nitrate reduction activity of layered perovskite oxide La_2CuO_4 via B-site doping, *Catal. Today* 402 (2022) 259–265, <https://doi.org/10.1016/j.cattod.2022.04.019>.
- [3] Z. Deng, C. Ma, Z. Li, Y. Luo, L. Zhang, S. Sun, Q. Liu, J. Du, Q. Lu, B. Zheng, X. Sun, High-efficiency electrochemical nitrate reduction to ammonia on a Co_3O_4 nanoarray catalyst with cobalt vacancies, *ACS Appl. Mater. Interfaces* 14 (41) (2022) 46595–46602, <https://doi.org/10.1021/acsami.2c12772>.
- [4] S. Li, P. Ma, C. Gao, L. Liu, X. Wang, M. Shakouri, R. Chernikov, K. Wang, D. Liu, R. Ma, J. Wang, Reconstruction-induced NiCu-based catalysts towards paired electrochemical refining, *Energy Environ. Sci.* 15 (7) (2022) 3004–3014, <https://doi.org/10.1039/D2EE00461E>.
- [5] J. Feng, H. Pan, Electronic state optimization for electrochemical N_2 reduction reaction in aqueous solution, *J. Mater. Chem. A* 8 (28) (2020) 13896–13915, <https://doi.org/10.1039/D0TA04709K>.
- [6] D. Liu, M. Chen, X. Du, H. Ai, K.H. Lo, S. Wang, S. Chen, G. Xing, X. Wang, H. Pan, Development of electrocatalysts for efficient nitrogen reduction reaction under ambient condition, *Adv. Funct. Mater.* 31 (11) (2020) 2008983, <https://doi.org/10.1002/adfm.202008983>.
- [7] P. Shen, X. Li, Y. Luo, Y. Guo, X. Zhao, K. Chu, High-efficiency N_2 electroreduction enabled by Se-vacancy-rich WSe_{2-x} in water-in-salt electrolytes, *ACS Nano* 16 (5) (2022) 7915–7925, <https://doi.org/10.1021/acsnano.2c00596>.
- [8] L. Li, C. Tang, X. Cui, Y. Zheng, X. Wang, H. Xu, S. Zhang, T. Shao, K. Davey, S. Z. Qiao, Efficient nitrogen fixation to ammonia through integration of plasma oxidation with electrocatalytic reduction, *Angew. Chem. Int. Ed. Engl.* 60 (25) (2021) 14131–14137, <https://doi.org/10.1002/anie.202104394>.
- [9] J. Liu, Z. Yang, L. Yang, Y. Zhu, T. Xue, G. Xu, Rational design of yolk-shell NiCo_2O_4 @void/ NiCo_2S_4 nanospheres for effective enhancement in microwave absorption, *J. Alloy. Compd.* 853 (2021), 157403, <https://doi.org/10.1016/j.jallcom.2020.157403>.
- [10] C. Wang, L.-L. Gu, S.-Y. Qiu, J. Gao, Y.-C. Zhang, K.-X. Wang, J.-J. Zou, P.-J. Zuo, X.-D. Zhu, Modulating CoFe_2O_4 nanocube with oxygen vacancy and carbon wrapper towards enhanced electrocatalytic nitrogen reduction to ammonia, *Appl. Catal. B: Environ.* 297 (2021), 120452, <https://doi.org/10.1016/j.apcatb.2021.120452>.
- [11] E. Murphy, Y. Liu, I. Matanovic, S. Guo, P. Tieu, Y. Huang, A. Ly, S. Das, I. Zenyuk, X. Pan, E. Spörke, P. Atanassov, Highly durable and selective Fe- and Mo-based atomically dispersed electrocatalysts for nitrate reduction to ammonia via distinct and synergized NO_2 pathways, *ACS Catal.* 12 (11) (2022) 6651–6662, <https://doi.org/10.1021/acscatal.2c01367>.
- [12] T. Zhu, Q. Chen, P. Liao, W. Duan, S. Liang, Z. Yan, C. Feng, Single-atom Cu catalysts for enhanced electrocatalytic nitrate reduction with significant alleviation of nitrite production, *Small* 16 (49) (2020), e2004526, <https://doi.org/10.1002/smll.202004526>.
- [13] L. Xie, Q. Liu, S. Sun, L. Hu, L. Zhang, D. Zhao, Q. Liu, J. Chen, J. Li, L. Ouyang, A. A. Alshehri, M.S. Hamdy, Q. Kong, X. Sun, High-efficiency electrosynthesis of ammonia with selective reduction of nitrate in neutral media enabled by self-supported Mn_2CoO_4 nanoarray, *ACS Appl. Mater. Interfaces* 14 (29) (2022) 33242–33247, <https://doi.org/10.1021/acsami.2c07818>.
- [14] Z. Wang, C. Sun, X. Bai, Z. Wang, X. Yu, X. Tong, Z. Wang, H. Zhang, H. Pang, L. Zhou, W. Wu, Y. Liang, A. Khosla, Z. Zhao, Facile Synthesis of carbon nanobelts decorated with Cu and Pd for nitrate electroreduction to ammonia, *ACS Appl. Mater. Interfaces* 14 (27) (2022) 30969–30978, <https://doi.org/10.1021/acsami.2c09357>.
- [15] Y. Wang, L. Zhang, Y. Niu, D. Fang, J. Wang, Q. Su, C. Wang, Boosting NH_3 production from nitrate electroreduction via electronic structure engineering of Fe_3C nanoflakes, *Green. Chem.* 23 (19) (2021) 7594–7608, <https://doi.org/10.1039/D1GC01913A>.
- [16] Y. Wang, A. Xu, Z. Wang, L. Huang, J. Li, F. Li, J. Wicks, M. Luo, D.H. Nam, C. S. Tan, Y. Ding, J. Wu, Y. Lum, C.T. Dinh, D. Sinton, G. Zheng, E.H. Sargent, Enhanced nitrate-to-ammonia activity on copper-nickel alloys via tuning of intermediate adsorption, *J. Am. Chem. Soc.* 142 (12) (2020) 5702–5708, <https://doi.org/10.1021/jacs.9b13347>.
- [17] J. Crawford, H. Yin, A. Du, A.P. O'Mullane, Nitrate-to-ammonia conversion at an InSn-enriched liquid-metal electrode, *Angew. Chem. Int. Ed.* 61 (23) (2022), e202201604, <https://doi.org/10.1002/anie.202201604>.
- [18] J. Wang, C. Cai, Y. Wang, X. Yang, D. Wu, Y. Zhu, M. Li, M. Gu, M. Shao, Electrocatalytic reduction of nitrate to ammonia on low-cost ultrathin CoO_x nanosheets, *ACS Catal.* 11 (24) (2021) 15135–15140, <https://doi.org/10.1021/acscatal.1c03918>.
- [19] C. Wang, F. Ye, J. Shen, K.H. Xue, Y. Zhu, C. Li, In situ loading of Cu_2O active sites on island-like copper for efficient electrochemical reduction of nitrate to ammonia, *ACS Appl. Mater. Interfaces* 14 (5) (2022) 6680–6688, <https://doi.org/10.1021/acsami.1c21691>.
- [20] J. Li, D. Zhao, L. Zhang, L. Yue, Y. Luo, Q. Liu, N. Li, A.A. Alshehri, M.S. Hamdy, Q. Li, X. Sun, A. FeCo_2O_4 nanowire array enabled electrochemical nitrate conversion to ammonia, *Chem. Commun.* 58 (28) (2022) 4480–4483, <https://doi.org/10.1039/D2CC00189F>.
- [21] W. Fu, X. Du, P. Su, Q. Zhang, M. Zhou, Synergistic effect of Co(III) and Co(II) in a 3D structured Co_3O_4 /carbon felt electrode for enhanced electrochemical nitrate reduction reaction, *ACS Appl. Mater. Interfaces* 13 (24) (2021) 28348–28358, <https://doi.org/10.1021/acsami.1c07063>.
- [22] X. Fan, C. Ma, D. Zhao, Z. Deng, L. Zhang, Y. Wang, Y. Luo, D. Zheng, T. Li, J. Zhang, S. Sun, Q. Lu, X. Sun, Unveiling selective nitrate reduction to ammonia with Co_3O_4 nanosheets/ TiO_2 nanobelt heterostructure catalyst, *J. Colloid Interface Sci.* 630 (2023) 714–720, <https://doi.org/10.1016/j.jcis.2022.10.050>.
- [23] J. Zhou, F. Pan, Q. Yao, Y. Zhu, H. Ma, J. Niu, J. Xie, Achieving efficient and stable electrochemical nitrate removal by in-situ reconstruction of $\text{Cu}_2\text{O}/\text{Cu}$ electroactive nanocatalysts on Cu foam, *Appl. Catal. B: Environ.* 317 (2022), 121811, <https://doi.org/10.1016/j.apcatb.2022.121811>.
- [24] D. Zhao, J. Liang, J. Li, L. Zhang, K. Dong, L. Yue, Y. Luo, Y. Ren, Q. Liu, M. S. Hamdy, Q. Li, Q. Kong, X. Sun, A. TiO_{2-x} nanobelt array with oxygen vacancies: an efficient electrocatalyst toward nitrite conversion to ammonia, *Chem. Commun.* 58 (22) (2022) 3669–3672, <https://doi.org/10.1039/d2cc00856d>.

- [25] D. Liu, L. Qiao, Y. Chen, P. Zhou, J. Feng, C.C. Leong, K.W. Ng, S. Peng, S. Wang, W.F. Ip, H. Pan, Electrocatalytic reduction of nitrate to ammonia on low-cost manganese-incorporated Co_3O_4 nanotubes, *Appl. Catal. B: Environ.* 324 (2023), 122293, <https://doi.org/10.1016/j.apcatb.2022.122293>.
- [26] Y.-T. Xu, M.-Y. Xie, H. Zhong, Y. Cao, In situ clustering of single-atom copper precatalysts in a metal-organic framework for efficient electrocatalytic nitrate-to-ammonia reduction, *ACS Catal.* 12 (14) (2022) 8698–8706, <https://doi.org/10.1021/acscatal.2c02033>.
- [27] P. Wei, J. Liang, Q. Liu, L. Xie, X. Tong, Y. Ren, T. Li, Y. Luo, N. Li, B. Tang, A. M. Asiri, M.S. Hamdy, Q. Kong, X. Sun, Iron-doped cobalt oxide nanoarray for efficient electrocatalytic nitrate-to-ammonia conversion, *J. Colloid Interface Sci.* 615 (2022) 636–642, <https://doi.org/10.1016/j.jcis.2022.01.186>.
- [28] Q. Liu, L. Xie, J. Liang, Y. Ren, Y. Wang, L. Zhang, L. Yue, T. Li, Y. Luo, N. Li, B. Tang, Y. Liu, S. Gao, A.A. Alshehri, I. Shakir, P.O. Agboola, Q. Kong, Q. Wang, D. Ma, X. Sun, Ambient ammonia synthesis via electrochemical reduction of nitrate enabled by $\text{NiCo}_2(\text{O})_4$ nanowire array, *Small* 18 (13) (2022), e2106961, <https://doi.org/10.1002/smll.202106961>.
- [29] Z. Li, J. Liang, Q. Liu, L. Xie, L. Zhang, Y. Ren, L. Yue, N. Li, B. Tang, A.A. Alshehri, M.S. Hamdy, Y. Luo, Q. Kong, X. Sun, High-efficiency ammonia electrosynthesis via selective reduction of nitrate on ZnCo_2O_4 nanosheet array, *Mater. Today Phys.* 23 (2022), 100619, <https://doi.org/10.1016/j.mtphys.2022.100619>.
- [30] P. Huang, T. Fan, X. Ma, J. Zhang, Y. Zhang, Z. Chen, X. Yi, 3D flower-like zinc cobaltite for electrocatalytic reduction of nitrate to ammonia under ambient conditions, *ChemSusChem* 15 (4) (2022), e202102049, <https://doi.org/10.1002/cssc.202102049>.
- [31] Z. Deng, J. Liang, Q. Liu, C. Ma, L. Xie, L. Yue, Y. Ren, T. Li, Y. Luo, N. Li, B. Tang, A. Ali Alshehri, I. Shakir, P.O. Agboola, S. Yan, B. Zheng, J. Du, Q. Kong, X. Sun, High-efficiency ammonia electrosynthesis on self-supported Co_2AlO_4 nanoarray in neutral media by selective reduction of nitrate, *Chem. Eng. J.* 435 (2022), 135104, <https://doi.org/10.1016/j.cej.2022.135104>.
- [32] X. Xu, L. Hu, Z. Li, L. Xie, S. Sun, L. Zhang, J. Li, Y. Luo, X. Yan, M.S. Hamdy, Q. Kong, X. Sun, Q. Liu, Oxygen vacancies in Co_3O_4 nanoarrays promote nitrate electroreduction for ammonia synthesis, *Sustainable Energy Fuels* 6 (18) (2022) 4130–4136, <https://doi.org/10.1039/D2SE00830K>.
- [33] L. Wen, X. Li, R. Zhang, H. Liang, Q. Zhang, C. Su, Y.J. Zeng, Oxygen vacancy engineering of MOF-derived Zn-doped $\text{Co}_3(\text{O})_4$ nanopolyhedrons for enhanced electrochemical nitrogen fixation, *ACS Appl. Mater. Interfaces* 13 (12) (2021) 14181–14188, <https://doi.org/10.1021/acscami.0c22767>.
- [34] J. Gao, B. Jiang, C. Ni, Y. Qi, X. Bi, Enhanced reduction of nitrate by noble metal-free electrocatalysis on P doped three-dimensional Co_3O_4 cathode: mechanism exploration from both experimental and DFT studies, *Chem. Eng. J.* 382 (2020), 123034, <https://doi.org/10.1016/j.cej.2019.123034>.
- [35] W. Fu, Z. Hu, Y. Du, P. Su, Y. Su, Q. Zhang, M. Zhou, Building dual active sites $\text{Co}_3\text{O}_4/\text{Cu}$ electrode to break scaling relations for enhancement of electrochemical reduction of nitrate to high-value ammonia, *J. Hazard Mater.* 434 (2022), 128887, <https://doi.org/10.1016/j.jhazmat.2022.128887>.
- [36] X. Du, J. Guo, M. Chen, W.-C. Cheong, Y. Chen, D. Liu, S. Chen, X. Wang, K. Ho Lo, J.-S. Hu, H. Pan, Surface reconstruction on silver nanoparticles decorated trimetallic hydroxide nanosheets to generate highly active oxygen-deficient (oxy) hydroxide layer for high-efficient water oxidation, *Chem. Eng. J.* 425 (2021), 131662, <https://doi.org/10.1016/j.cej.2021.131662>.
- [37] M. Chen, D. Liu, J. Feng, P. Zhou, L. Qiao, W. Feng, Y. Chen, K. Wei Ng, S. Wang, W. Fai Ip, H. Pan, In-situ generation of Ni-CoOOH through deep reconstruction for durable alkaline water electrolysis, *Chem. Eng. J.* 443 (2022), 136432, <https://doi.org/10.1016/j.cej.2022.136432>.
- [38] P. Zhou, P. Niu, J. Liu, N. Zhang, H. Bai, M. Chen, J. Feng, D. Liu, L. Wang, S. Chen, C.T. Kwok, Y. Tang, R. Li, S. Wang, H. Pan, Anodized steel: the most promising bifunctional electrocatalyst for alkaline water electrolysis in industry, *Adv. Funct. Mater.* 32 (26) (2022) 2202068, <https://doi.org/10.1002/adfm.202202068>.
- [39] L. Qiao, A. Zhu, D. Liu, J. Feng, Y. Chen, M. Chen, P. Zhou, L. Yin, R. Wu, K.W. Ng, H. Pan, Crystalline phosphides/amorphous oxides composite for energy-saving hydrogen production assisted by efficient urea oxidation reaction, *Chem. Eng. J.* 454 (2023), 140380, <https://doi.org/10.1016/j.cej.2022.140380>.
- [40] H.Y. Wang, S.F. Hung, H.Y. Chen, T.S. Chan, H.M. Chen, B. Liu, In operando identification of geometrical-site-dependent water oxidation activity of spinel Co_3O_4 , 36–9, *J. Am. Chem. Soc.* 138 (1) (2016), <https://doi.org/10.1021/jacs.5b10525>.
- [41] Y. Wang, W. Zhou, R. Jia, Y. Yu, B. Zhang, Unveiling the activity origin of a copper-based electrocatalyst for selective nitrate reduction to ammonia, *Angew. Chem. Int. Ed. Engl.* 59 (13) (2020) 5350–5354, <https://doi.org/10.1002/anie.201915992>.
- [42] S. Ye, Z. Chen, G. Zhang, W. Chen, C. Peng, X. Yang, L. Zheng, Y. Li, X. Ren, H. Cao, D. Xue, J. Qiu, Q. Zhang, J. Liu, Elucidating the activity, mechanism and application of selective electrosynthesis of ammonia from nitrate on cobalt phosphide, *Energy Environ. Sci.* 15 (2) (2022) 760–770, <https://doi.org/10.1039/D1EE03097C>.
- [43] Y. Gao, D. Zheng, Q. Li, W. Xiao, T. Ma, Y. Fu, Z. Wu, L. Wang, 3D $\text{Co}_3\text{O}_4\text{-RuO}_2$ hollow spheres with abundant interfaces as advanced trifunctional electrocatalyst for water-splitting and flexible Zn–Air battery, *Adv. Funct. Mater.* 32 (38) (2022) 2203206, <https://doi.org/10.1002/adfm.202203206>.
- [44] R. Ge, L. Li, J. Su, Y. Lin, Z. Tian, L. Chen, Ultrafine defective RuO_2 electrocatalyst integrated on carbon cloth for robust water oxidation in acidic media, *Adv. Energy Mater.* 9 (35) (2019) 1901313, <https://doi.org/10.1002/aenm.201901313>.
- [45] T. Xu, Z. Li, D. Wang, M. Zhang, L. Ai, Z. Chen, J. Zhang, X. Zhang, L. Shen, A fast proton-induced pseudocapacitive supercapacitor with high energy and power density, *Adv. Funct. Mater.* 32 (5) (2021) 2107720, <https://doi.org/10.1002/adfm.202107720>.
- [46] W. Zhong, C. Yang, J. Wu, W. Xu, R. Zhao, H. Xiang, K. Shen, Q. Zhang, X. Li, Oxygen vacancies induced by charge compensation tailoring Ni-doped Co_3O_4 nanoflakes for efficient hydrogen evolution, *Chem. Eng. J.* 436 (2022), 134813, <https://doi.org/10.1016/j.cej.2022.134813>.
- [47] H. Chen, C. Zhang, L. Sheng, M. Wang, W. Fu, S. Gao, Z. Zhang, S. Chen, R. Si, L. Wang, B. Yang, Copper single-atom catalyst as a high-performance electrocatalyst for nitrate-ammonium conversion, *J. Hazard Mater.* 434 (2022), 128892, <https://doi.org/10.1016/j.jhazmat.2022.128892>.
- [48] J. Rosen, G.S. Hutchings, F. Jiao, Ordered mesoporous cobalt oxide as highly efficient oxygen evolution catalyst, 4516–21, *J. Am. Chem. Soc.* 135 (11) (2013), <https://doi.org/10.1021/ja400555q>.
- [49] P. Xia, S. Cao, B. Zhu, M. Liu, M. Shi, J. Yu, Y. Zhang, Designing a 0D/2D S-scheme heterojunction over polymeric carbon nitride for visible-light photocatalytic inactivation of bacteria, *Angew. Chem. Int. Ed.* 59 (13) (2020) 5218–5225, <https://doi.org/10.1002/anie.201916012>.
- [50] K. Guo, Y. Wang, J. Huang, M. Lu, H. Li, Y. Peng, P. Xi, H. Zhang, J. Huang, S. Lu, C. Xu, In situ activated $\text{Co}_3\text{-xNi}_x\text{O}_4$ as a highly active and ultrastable electrocatalyst for hydrogen generation, *ACS Catal.* 11 (13) (2021) 8174–8182, <https://doi.org/10.1021/acscatal.1c01607>.
- [51] J. Li, R. Chen, J. Wang, Y. Zhou, G. Yang, F. Dong, Subnanometric alkaline-earth oxide clusters for sustainable nitrate to ammonia photosynthesis, *Nat. Commun.* 13 (1) (2022) 1098, <https://doi.org/10.1038/s41467-022-28740-8>.
- [52] H. Guo, M. Li, Y. Yang, R. Luo, W. Liu, F. Zhang, C. Tang, G. Yang, Y. Zhou, Self-supported Pd nanorod arrays for high-efficient nitrate electroreduction to ammonia, *Small* (2023), e2207743, <https://doi.org/10.1002/smll.202207743>.
- [53] W. Chen, L. Xu, X. Zhu, Y.C. Huang, W. Zhou, D. Wang, Y. Zhou, S. Du, Q. Li, C. Xie, L. Tao, C.L. Dong, J. Liu, Y. Wang, R. Chen, H. Su, C. Chen, Y. Zou, Y. Li, Q. Liu, S. Wang, Unveiling the electrooxidation of urea: intramolecular coupling of the N–N bond, *Angew. Chem. Int. Ed. Engl.* 60 (13) (2021) 7297–7307, <https://doi.org/10.1002/anie.202015773>.
- [54] J. Li, H.-X. Liu, W. Gou, M. Zhang, Z. Xia, S. Zhang, C.-R. Chang, Y. Ma, Y. Qu, Ethylene-glycol ligand environment facilitates highly efficient hydrogen evolution of Pt/CoP through proton concentration and hydrogen spillover, *Energy Environ. Sci.* 12 (7) (2019) 2298–2304, <https://doi.org/10.1039/C9EE00752K>.
- [55] Z. Xiao, Y.C. Huang, C.L. Dong, C. Xie, Z. Liu, S. Du, W. Chen, D. Yan, L. Tao, Z. Shu, G. Zhang, H. Duan, Y. Wang, Y. Zou, R. Chen, S. Wang, Operando identification of the dynamic behavior of oxygen vacancy-rich Co_3O_4 for oxygen evolution reaction, *J. Am. Chem. Soc.* 142 (28) (2020) 12087–12095, <https://doi.org/10.1021/jacs.0c00257>.
- [56] W. Xiang, N. Yang, X. Li, J. Linnemann, U. Hagemann, O. Ruediger, M. Heideilmann, T. Falk, M. Aramini, S. DeBeer, M. Muhler, K. Tschulik, T. Li, 3D atomic-scale imaging of mixed Co-Fe spinel oxide nanoparticles during oxygen evolution reaction, *Nat. Commun.* 13 (1) (2022) 179, <https://doi.org/10.1038/s41467-021-27788-2>.
- [57] T. Li, C. Tang, H. Guo, H. Wu, C. Duan, H. Wang, F. Zhang, Y. Cao, G. Yang, Y. Zhou, In situ growth of Fe_2O_3 nanorod arrays on carbon cloth with rapid charge transfer for efficient nitrate electroreduction to ammonia, *ACS Appl. Mater. Interfaces* 14 (44) (2022) 49765–49773, <https://doi.org/10.1021/acscami.2c14215>.
- [58] Z. Chang, G. Meng, Y. Chen, C. Chen, S. Han, P. Wu, L. Zhu, H. Tian, F. Kong, M. Wang, X. Cui, J. Shi, Dual-site W–O–CoP catalysts for active and selective nitrate conversion to ammonia in a broad concentration window, *Adv. Mater.* (2023), e2304508, <https://doi.org/10.1002/adma.202304508>.
- [59] X. Liu, R. Guo, K. Ni, F. Xia, C. Niu, B. Wen, J. Meng, P. Wu, J. Wu, X. Wu, L. Mai, Reconstruction-determined alkaline water electrolysis at industrial temperatures, *Adv. Mater.* 32 (40) (2020), e2001136, <https://doi.org/10.1002/adma.202001136>.
- [60] X. Liu, J. Meng, J. Zhu, M. Huang, B. Wen, R. Guo, L. Mai, Comprehensive understandings into complete reconstruction of precatalysts: synthesis, applications, and characterizations, *Adv. Mater.* 33 (32) (2021), e2007344, <https://doi.org/10.1002/adma.202007344>.
- [61] X. Han, H. Sheng, C. Yu, T.W. Walker, G.W. Huber, J. Qiu, S. Jin, Electrocatalytic oxidation of glycerol to formic acid by CuCo_2O_4 spinel oxide nanostructure catalysts, *ACS Catal.* 10 (12) (2020) 6741–6752, <https://doi.org/10.1021/acscatal.0c01498>.
- [62] Y.-C. Liu, J.A. Koza, J.A. Switzer, Conversion of electrodeposited $\text{Co}(\text{OH})_2$ to CoOOH and Co_3O_4 , and comparison of their catalytic activity for the oxygen evolution reaction, *Electrochim. Acta* 140 (2014) 359–365, <https://doi.org/10.1016/j.electacta.2014.04.036>.
- [63] S. Mo, Q. Zhang, S. Li, Q. Ren, M. Zhang, Y. Xue, R. Peng, H. Xiao, Y. Chen, D. Ye, Integrated cobalt oxide based nanoarray catalysts with hierarchical architectures: in situ Raman spectroscopy investigation on the carbon monoxide reaction mechanism, *ChemCatChem* 10 (14) (2018) 3012–3026, <https://doi.org/10.1002/cctc.201800363>.